POLITECNICO DI TORINO
Repository ISTITUZIONALE

Effect of carbon quantum dots on the UV-curing behavior and properties of waterborne polyurethane acrylate coatings

Original
Effect of carbon quantum dots on the UV-curing behavior and properties of waterborne polyurethane acrylate coatings / Dall Agnol, L., De Medeiros Brandão, M.G., Correia, G.S., Dias, F.T.G., Sangermano, M., Bianchi, O.. - In: POLYMER BULLETIN. - ISSN 0170-0839. - ELETTRONICO. - 83:12(2026), pp. 1-30. [10.1007/s00289-026-06712-y]

Availability:
This version is available at: 11583/3016445 since: 2026-10-09T06:50:11Z

Publisher:
Springer

Published
DOI:10.1007/s00289-026-06712-y

Terms of use:

This article is made available under terms and conditions as specified in the corresponding bibliographic description in the repository

Publisher copyright

(Article begins on next page)

19 November 2026

Polymer Bulletin (2026) 83:675
https://doi.org/10.1007/s00289-026-06712-y

ORIGINAL PAPER

Effect of carbon quantum dots on the UV-curing behavior and properties of waterborne polyurethane acrylate coatings

Lucas Dall Agnol[1,2] · Marcos Gustavo de Medeiros Brandão[1] · Gricirene Sousa Correia[1] · Fernanda Trindade Gonzalez Dias[3] · Marco Sangermano[4] · Otávio Bianchi[2]

Received: 21 April 2026 / Revised: 8 July 2026 / Accepted: 21 September 2026
© The Author(s) 2026

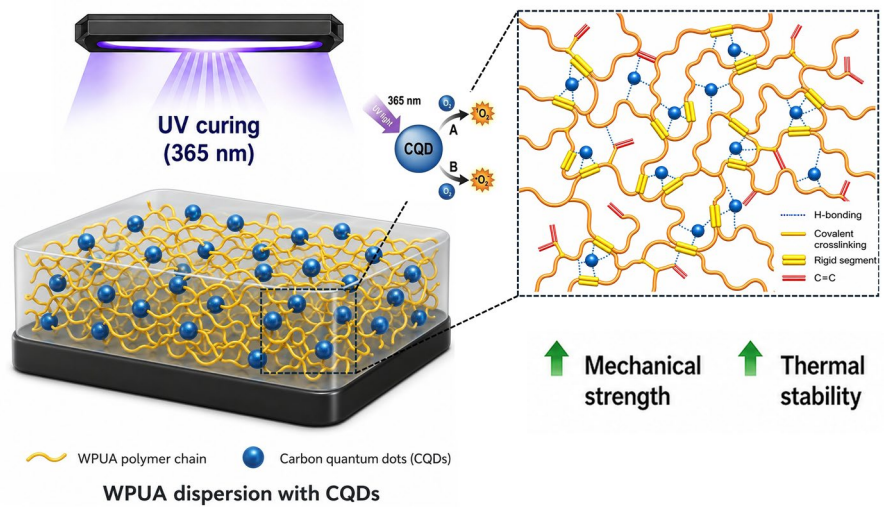
Abstract

Photoactive carbon quantum dots (CQDs) are promising modifiers for waterborne polyurethane acrylate (WPUA) coatings, but their effect on UV-curing kinetics depends on how they interact with the photopolymerizable matrix. This study evaluates the influence of CQDs surface chemistry, photoluminescence quantum yield (QY), and incorporation route on curing behavior and final coating properties. Two CQDs with distinct QY values (≈23% and ≈62%) but similar surface functional groups were incorporated into WPUA dispersions via aqueous-phase addition and acetone pre-dispersion. Photo-DSC analysis revealed that CQDs broadened curing profiles, increased peak time from 4.2 s to 13.7–44.5 s, and reduced C=C conversion from 92.8% to 50.8–77.9%. A semi-quantitative analysis indicated that curing retardation arises from combined competitive UV absorption and route-dependent mobility restrictions induced by CQDs–WPUA interactions. Despite reduced conversion and gel content (97.8% to 83–93%), CQDs improved coating performance, increasing tensile strength from 4.3 MPa to 6.1–6.6 MPa (≈40–53%), and thermal stability ($T_{10\%}$) from 298.2 °C to 309.1 °C. The incorporation route affected curing and properties in a CQDs-dependent manner, while QY differences produced only minor kinetic effects, indicating that surface chemistry and matrix interactions govern the response more strongly than photoluminescence. Under air, selected formulations suggested an apparent attenuation of oxygen inhibition, consistent with auxiliary CQDs photoactivity. Hansen solubility parameter analysis further revealed a contraction of the solubility sphere, indicating a more constrained network with improved solvent resistance. CQDs act as multifunctional modifiers that tune curing efficiency and coating performance through surface functionality and incorporation route.

Extended author information available on the last page of the article

Published online: 07 October 2026

Graphical abstract



Keywords Carbon quantum dots · Waterborne polyurethane acrylate · UV-curable coatings · Photopolymerization kinetics · Hansen solubility parameters

Introduction

Growing environmental awareness and steadily tightening regulations on volatile organic compound (VOC) emissions have accelerated the global transition from solvent-borne to more sustainable coating technologies [1]. Within this frame, ultraviolet (UV) curing has emerged as a compelling alternative because it enables rapid film formation with reduced energy demand and, when properly formulated, a substantially lower environmental footprint relative to conventional thermally cured systems [2]. Under irradiation by a suitable light source, UV-curable formulations generate highly crosslinked networks within seconds to minutes, delivering coatings with high hardness, chemical resistance, and robust mechanical performance [3–5]. Nevertheless, many UV-curable systems still rely on reactive diluents or low-molecular-weight monomers to achieve workable viscosities, raising concerns about volatility, odor, skin sensitization, and potential toxicity [6]. Consequently, designing UV-curable coating platforms that maintain high performance while minimizing VOC-related risks remains a central challenge in modern surface-coating technologies.

Waterborne polyurethane acrylates (WPUA) represent a particularly promising class of materials that combine the advantages of aqueous polymer dispersions with the rapid curing capability of UV-induced free-radical photopolymerization [1, 7]. In these systems, polyurethane chains bearing pendant acrylate groups undergo crosslinking under UV irradiation, forming networks with enhanced mechanical strength, thermal stability, and chemical resistance. Because water serves as the continuous phase, WPUA systems exhibit significantly lower VOC emissions than their solvent-

borne counterparts [8]. For these reasons, UV-curable WPUA coatings have been widely explored for applications in wood finishing, electronics, printing inks, textile finishing, and industrial protective coatings [4, 9]. The curing behavior and final properties of WPUA systems, however, are strongly dependent on formulation parameters such as photoinitiator concentration, oligomer functionality, dispersion particle size, and the presence of additives or nanostructured fillers [1].

One important limitation of conventional UV-curable formulations is their reliance on organic photoinitiators to generate reactive radicals upon irradiation [1]. Although photoinitiators are effective in initiating polymerization, their photolysis can produce low-molecular-weight fragments that may volatilize, migrate to the coating surface, or become permanently entrapped within the cured matrix, raising long-term environmental and toxicological concerns [6, 10]. These limitations have motivated considerable research into alternative or complementary strategies, including the incorporation of functional nanomaterials that can modulate light absorption, participate in radical generation, and influence network formation during UV curing [1, 8]. Several inorganic UV-active nanoparticles, including TiO_2 nanorods, ZnO nanoparticles, and carbon nanotubes, have been incorporated into photocurable matrices to explore multifunctional roles [8, 11, 12]. However, concerns about their cytotoxicity, poor dispersibility in aqueous media, and limited tunability of surface chemistry have motivated the search for carbon-based alternatives.

Carbon quantum dots (CQDs) have emerged as a versatile class of carbon-based nanomaterials with unique and tunable optical and physicochemical properties [13]. CQDs are nanoscale carbon particles, generally smaller than 10 nm, that exhibit strong photoluminescence, excellent photostability, low cytotoxicity, and an abundance of surface functional groups (including hydroxyl, carboxyl, and amine moieties) that confer good dispersibility in aqueous media and promote interfacial interactions with polar polymer matrices [14]. Under UV irradiation, CQDs can participate in photoredox processes, acting both as electron donors and acceptors, and have been shown to generate reactive oxygen species (ROS), including singlet oxygen ($^1O_2$) and superoxide anion radicals ($O_2^{\bullet -}$), via energy-transfer mechanisms [9, 15]. These photochemical properties suggest that CQDs may actively modulate free-radical polymerization when incorporated into UV-curable formulations, a hypothesis that has been only partially investigated, particularly in waterborne systems.

The few studies that have incorporated CQDs into photopolymerizable matrices have primarily focused on demonstrating property improvements, such as enhanced photoluminescence, antibacterial activity, or mechanical reinforcement [1], without providing mechanistic insight into how CQDs properties govern curing kinetics. Crucially, no prior work has attempted to decouple the contributions of photoluminescence quantum yield (QY) from those of surface functional group chemistry on the photopolymerization behavior of a WPUA system. This distinction is not merely academic: it has direct implications for CQDs materials design, since photoluminescence and surface chemistry can be independently tuned through precursor selection and the synthesis route. Furthermore, the stage at which nanoparticles are introduced into a waterborne polyurethane dispersion, whether during prepolymer formation, prior to phase inversion, or during aqueous dispersion, profoundly affects the degree

of nanoparticle–polymer coupling achieved. Nevertheless, this process parameter has been largely overlooked in the WPUA nanocomposite literature [16].

Additionally, the effect of oxygen on CQDs-containing UV-curable systems remains largely unexplored. In conventional free-radical photopolymerization, atmospheric oxygen acts as a potent radical scavenger, forming low-reactivity peroxy radicals that reduce propagation efficiency and final conversion, especially in thin coatings [17]. Given that CQDs generate ROS under UV irradiation, they may partially compensate for this inhibitory effect by providing auxiliary radical sources, a possibility that has not been examined in waterborne photopolymerizable formulations. To address these open questions, the present work investigated the influence of two structurally distinct CQDs (CQD-Eda − derived from citric acid and ethylenediamine, QY ≈ 62%; and CQD-Spr − derived from Spirulina biomass, QY ≈ 23%) on the UV-curing behavior and physicochemical properties of WPUA coatings.

The two types of CQDs exhibited similar surface functional group compositions but substantially different quantum yields, enabling, for the first time in a WPUA system, a direct experimental comparison that decouples the effects of optical emission characteristics from those of interfacial chemistry on photopolymerization kinetics. Special attention was given to: (i) how CQDs surface chemistry and photoluminescent properties modulate curing kinetics as assessed by photo-differential scanning calorimetry (photo-DSC); (ii) how the nanoparticle dispersion route (aqueous phase addition *versus* organic solvent pre-dispersion prior to phase inversion) controls the extent of polymer–nanoparticle coupling and its downstream consequences for mechanical performance, thermal stability, and solvent resistance; and (iii) whether CQDs can attenuate oxygen inhibition through photosensitized ROS generation under UV irradiation. The results are expected to provide mechanistic insights into the dual role of CQDs as both passive nanofillers and photochemically active species, and to establish rational design guidelines for CQDs-containing UV-curable waterborne coating formulations.

Materials and methods

Materials

Polycaprolactone diol (PCL, *Mw* = 2000 g/mol, hydroxyl value 56.3 mg·KOH/g), hexamethylene diisocyanate (HDI, ≥ 99% purity), 2,2-bis(hydroxymethyl)propionic acid (DMPA, 98%), dibutyltin dilaurate (DBTDL, 95%), methyl ethyl ketone (MEK), triethylamine (TEA, ≥ 99.5%), pentaerythritol triacrylate (PETA), 2-hydroxy-4′-(2-hydroxyethoxy)−2-methylpropiophenone (Irgacure 2959®), ethylenediamine (EDA, ≥ 99.5%), citric acid (CA, 98.5%) and quinine sulfate (≥98%, used as a fluorescence quantum yield standard) were obtained from Sigma-Aldrich (USA). Dried Spirulina biomass in powder form was supplied by Galena Química e Farmacêutica LTDA (Campinas, Brazil). Prior to use, DMPA and PCL were dried under vacuum (1330 Pa) at 90 °C for 4 h to remove residual moisture, which could interfere with the isocyanate reactions during prepolymer synthesis. All solvents were of analytical grade and used as received. Ultrapure water (≥18.25 MΩ·cm) was used in all experiments.

Synthesis of CQDs

Different routes synthesized two types of CQDs with distinct photoluminescent properties to evaluate the influence of their surface chemistry and optical characteristics on the UV-curing behavior of the waterborne polyurethane acrylate (WPUA) matrix. The first type, denoted CQD-*Eda*, was prepared by microwave-assisted pyrolysis of CA and EDA, following the procedure reported by Dall Agnol et al. (2023) [9]. The second type, denoted CQD-*Spr,* was obtained by thermal pyrolysis of Spirulina biomass at 300 °C for 2 h using a heating rate of 10 °C/min, as described by Dall Agnol et al. (2021) [14]. The use of two distinct precursor systems, one synthetic (CQD-*Eda*) and another biobased (CQD-*Spr*), was intended to produce CQDs with different surface functional group densities, nitrogen contents, and quantum yields, thereby allowing an independent assessment of the role of photoluminescent properties *versus* surface chemistry on the photopolymerization behavior of the WPUA system.

Synthesis of WPUA/CQDs nanocomposites

WPUA/CQDs nanocomposites were synthesized in a dry four-necked flask equipped with a mechanical stirrer, reflux condenser, oil bath, dropping funnel, and nitrogen inlet. Briefly, PCL and HDI were reacted in the presence of DBTDL catalyst (0.03 wt.% relative to total HDI and PCL) at 80 °C for 4 h under a nitrogen atmosphere and constant stirring (180 rpm) to yield an isocyanate-terminated (–NCO) prepolymer. An inert atmosphere was necessary to prevent moisture-induced side reactions with the isocyanate groups. Subsequently, DMPA was added, and the reaction was continued at 80 °C for an additional 2 h. MEK was introduced to control the viscosity of the medium throughout the synthesis. PETA was then added as the acrylate functional crosslinker, and the reaction was extended for 3 h until the –NCO absorption band (approximately 2270 cm^{-1}) had essentially disappeared, as monitored by FTIR spectroscopy. The reaction temperature was subsequently reduced to 45 °C, and TEA was added to neutralize the –COOH groups of the prepolymer over 45 min, yielding an ionomer that could be dispersed in water. Phase inversion was then performed by dispersing the neutralized prepolymer under vigorous stirring (1100 rpm) for 30 min into either (i) aqueous solutions containing 1.0 wt% CQDs (CQD-Eda or CQD-Spr), or (ii) pure water, when the CQDs had been pre-dispersed in acetone and incorporated into the system prior to phase inversion. A CQDs-free formulation (0.0 wt.%) was also prepared as the reference sample. The stoichiometric molar ratio employed was HDI/PCL/DMPA/PETA/TEA = 3.5:1:1:1:1.2, corresponding to an NCO/OH index slightly above stoichiometry to ensure complete urethane bond formation and maximize acrylate end-capping efficiency. Residual solvents were removed by distillation under reduced pressure at 60 °C for 2 h. The solid content of the resulting dispersions was approximately 30 wt.%. The complete experimental design is summarized in Table 1.

Table 1 Composition of the WPUA-based formulations as a function of CQDs type, content, incorporation stage, and photoinitiator addition

Sample ID	CQDs type	CQDs content (wt.%)	Photoinitiator (3.0 wt.%)	CQDs addition step
WPUA-0^{+}	-	0.0	Yes	-
WPUA-0^{-}	-	0.0	No	
WPUA-$Eda_{(aq^{+})}$	CQD-*Eda*	1.0	Yes	Dispersed in aqueous phase (during phase inversion)
WPUA-$Eda_{(aq-)}$	CQD-*Eda*	1.0	No	
WPUA-$Spr_{(aq^{+})}$	CQD-*Spr*	1.0	Yes	
WPUA-$Spr_{(aq-)}$	CQD-*Spr*	1.0	No	
WPUA-$Eda_{(ac+)}$	CQD-*Eda*	1.0	Yes	Dispersed in acetone prior to phase inversion
WPUA-$Eda_{(ac-)}$	CQD-*Eda*	1.0	No	
WPUA-$Spr_{(ac+)}$	CQD-*Spr*	1.0	Yes	
WPUA-$Spr_{(ac-)}$	CQD-*Spr*	1.0	No	

CQD-Eda and CQD-Spr identify the CQDs prepared from CA/EDA and Spirulina biomass, respectively. In the sample IDs, "aq" indicates addition to the aqueous phase during phase inversion, and "ac" indicates dispersion in acetone before phase inversion. The symbols "+" and "–" indicate the presence and absence of photoinitiator, respectively (3.0 wt.% when present). Boldface and italics have no additional experimental significance

Preparation of UV-cured films

After synthesis, the photoinitiator Irgacure 2959® was added to the prepared dispersions at a concentration of 3.0 wt% relative to the ionomer content, and the mixture was mixed for 5 min. Films were cast onto Teflon plates, dried at room temperature in the dark for 24 h, and then at 40 °C for 72 h. Control films without a photoinitiator were also prepared to evaluate the CQDs' intrinsic photochemical activity. The dried films (average thickness ≈ 30 μm) were irradiated at room temperature under a 100 W UV-lamp (365 nm) for 2 min.

Structural analysis and photoluminescent properties of CQDs

Fourier transform infrared (FTIR) spectra were recorded on a Perkin Elmer Impact 400 spectrometer over the wavenumber range of 4000–400 cm^{-1}, using 64 scans at a resolution of 4 cm^{-1}. All measurements were performed in attenuated total reflectance (ATR) mode using a diamond crystal positioned at a 45° incidence angle. UV–Vis absorption spectra were obtained using an Evolution 60S spectrophotometer (Thermo Scientific) over the wavelength range of 200–600 nm. Photoluminescence emission spectra were recorded using a PerkinElmer LS 45 fluorescence spectrometer with a fixed excitation wavelength of 360 nm; emission was collected from 350 to 600 nm. A quartz cuvette with a 1 cm optical path length was used for all optical measurements. The photoluminescence quantum yield (QY) of each type of CQDs was estimated by a relative method, comparing the integrated PL emission intensity and the absorbance at 360 nm of the CQDs dispersions against those of a quinine sulfate reference solution (0.1 M H_2SO_4, QY = 54%) at progressively increasing concentrations, as described in Ref. [14]. Hydrodynamic particle size distributions

were determined at 25 °C by dynamic light scattering (DLS) using a Delsa™ Nano Series analyzer (Beckman Coulter) equipped with a 30 mW diode laser (λ = 658 nm) operating at a fixed scattering angle of 165°.

Characterization of WPUA/CQDs nanocomposites

Chemical structure

The chemical structure of the neat WPUA and WPUA/CQDs nanocomposite films, both before and after UV curing, was evaluated by FTIR spectroscopy using a PerkinElmer Impact 400 spectrometer (4000–400 cm^{-1}, 64 scans, resolution of 4 cm^{-1}) in ATR mode (ATR, diamond crystal at 45º). The reduction in the intensity of the C=C stretching band at approximately 1640 cm^{-1} and the out-of-plane bending vibration of the acrylate group at 810 cm^{-1} upon UV irradiation were used as qualitative indicators of the photopolymerization degree. Differences in the FTIR profiles of the CQDs-containing films were analyzed to assess potential interactions between the nanoparticle surface groups and the WPUA matrix.

UV-curing behavior by photo-differential scanning calorimetry (photo-DSC)

The UV-curing behavior of the formulations was characterized by photo-DSC using a DSC Q2000 calorimeter (TA Instruments) coupled to a photocalorimetric accessory (Omnicure S2000) equipped with a 100 W mercury arc lamp operating in the 320–500 nm wavelength range. The incident light intensity at the sample surface was calibrated to 50 mW/cm^2 prior to the experiments. Approximately 5 mg of each uncured film was placed in an open aluminum pan and analyzed isothermally at 25 °C under a continuous flow (50 mL/min) of either dry nitrogen (inert atmosphere) or compressed air (oxidative atmosphere). The use of two distinct curing atmospheres was intended to evaluate the role of oxygen in the photopolymerization process and the potential of CQDs to generate radicals via reactive oxygen species. The degree of C=C double bond conversion (α) at time *t* was calculated from the ratio of the measured reaction enthalpy to the theoretical enthalpy for complete conversion, according to Eq. 1 [3].

$$\alpha = \frac{\Delta H_t}{\Delta H_0^{theor}} \tag{1}$$

where ΔH_t is the exothermic enthalpy released up to time *t*, and ΔH_0^{theor} is the theoretical enthalpy for full acrylate conversion, estimated from Eq. 2:

$$\Delta H_0^{theor} = \frac{86 \times Functionality}{M_w^{theor}} \tag{2}$$

where M_w^{theor} is the theoretical molecular weight of the prepolymer, 86 kJ/mol is the theoretical enthalpy released by the complete polymerization of one mole of acrylate C=C bonds, as commonly adopted in Photo-DSC studies of acrylate-based systems

[4], and *f* is the acrylate functionality, considered as 3 due to the three acrylate groups of PETA. The instantaneous polymerization rate (R_p) was obtained from Eq. 3.

$$R_p = \frac{d\alpha}{dt} = \frac{(dH/dt)}{\Delta H_0^{theor}} \tag{3}$$

where $d\alpha/dt$ is the rate of conversion, and dH/dt is the heat flow measured by the calorimeter at constant temperature. The time of the maximum heat flow (peak) and the total enthalpy of the exothermic event (ΔH) were also recorded as additional parameters to characterize the curing profiles of the different formulations.

Gel content

The gel content of the UV-cured films was determined by Soxhlet extraction into toluene, following a standard gravimetric procedure. After irradiation, the films were cut into 2 cm × 2 cm pieces and weighed (initial dry weight, W_0). The specimens were then placed in baskets made of 200-mesh stainless steel net and subjected to continuous extraction in toluene for 48 h at the solvent reflux temperature, approximately 110 °C, to remove the soluble uncrosslinked fraction. After extraction, the samples were dried at 30 °C for 72 h and reweighed (W_2). The gel content (%) was calculated according to Eq. 4:

$$\%Gel = \frac{w_2}{w_0} \times 100\% \tag{4}$$

Thermal characterization

The thermal behavior of the nanocomposite films was evaluated by differential scanning calorimetry (DSC) and thermogravimetric analysis (TGA). DSC measurements were performed on a DSC Q2000 (TA Instruments) under a nitrogen atmosphere (50 mL/min) and a heating rate of 10 °C/min. Samples of 10–15 mg were sealed in hermetic aluminum crucibles and subjected to the following thermal program: first heating from −80 °C to 200 °C, isothermal hold at 200 °C for 3 min (to erase thermal history), cooling to −80 °C, isothermal hold for 3 min, and second heating to 200 °C. Thermal transitions were identified from the second heating scan to ensure the elimination of any residual stress or physical aging effects. The glass transition temperatures of the soft-segment (T_{gSS}) and the relaxation enthalpy of the hard-segment domains (T_{hd}) were determined from the midpoint of the heat capacity step and the peak position of the endothermic transition, respectively.

TGA measurements were carried out using a TGA-50 instrument (Shimadzu) over the temperature range of 25–800 ºC, under a N_2 atmosphere (50 mL/min) and a heating rate of 10 °C/min. The temperatures corresponding to 10% and 50% weight loss ($T_{10\%}$ and $T_{50\%}$) were used as reference parameters to assess the onset of thermal degradation and the midpoint of the main decomposition stage, respectively. The residual char yield at 800 °C was also recorded as an indicator of carbonaceous residue formation, which is particularly relevant for CQDs-containing systems.

Mechanical properties

Tensile properties, including tensile strength (σ_{max}) and elongation at break (ε_b), were determined using an Emic DL2000 universal testing machine equipped with a 500 N load cell at a crosshead speed of 100 mm/min, in accordance with ASTM D638. Specimens with nominal dimensions of 100 × 10 × 3 mm were tested. Shore A hardness was determined according to ASTM D2240 using a Bareiss analog durometer on 6 mm-thick compression-molded plates, with a contact time of 3 s per reading. All mechanical tests were conducted at 23 ºC using a minimum of five specimens per formulation, and the results were reported as mean ± standard deviation. Statistical analysis was performed using the individual replicate values. Differences among formulations were evaluated by one-way analysis of variance (ANOVA) followed by Tukey's post hoc test, considering a significance level of $p<0.05$. Statistical comparisons were performed independently for each property.

Swelling behavior

Water uptake was evaluated as a measure of the hydrophilicity and swelling resistance of the cured films. Three specimens per formulation (20 cm × 20 cm × 30 µm) were dried in a circulating air oven at 60 °C for 48 h to obtain the initial dry weight (W_d). The dried specimens were then immersed in distilled water at room temperature, and the wet weight (W_w) was recorded after 48 h. Excess surface water was removed with absorbent paper immediately before weighing. Water uptake (*WU, %*) was calculated using Eq. (5):

$$WU = \frac{W_w - W_d}{W_d}.100\% \tag{5}$$

Higher water uptake values indicate a more hydrophilic network, which can result from lower crosslinking density, the presence of unreacted hydrophilic groups, or the incorporation of polar nanoparticles. Results are reported as mean ± standard deviation of triplicate measurements.

Surface free energy

The surface free energy (γ_S) of the cured films was evaluated using the Owens–Wendt method [18]. Static contact angles were measured with a SEO® Phoenix100 (Korea) goniometer at 23 ± 2 °C, using four probe liquids with well-characterized surface tension (γ_L), dispersive (non-polar) (γ_L^D), and polar (γ_L^P) components [9]: distilled water, diethylene glycol, dimethyl sulfoxide (DMSO), and hexadecane. These liquids were selected to provide a range of polar and non-polar interactions, enabling reliable fitting of the Owens–Wendt equation. Droplet volumes were fixed at 2 µL to minimize gravitational deformation of the sessile drop. Contact angles were measured at a minimum of 10 independent locations on each film surface, and average values were used to calculate surface energy components.

Hansen solubility parameters (HSP)

The HSP of selected cured films was determined using a solvent screening approach with a set of 34 solvents spanning a wide range of physicochemical characteristics, including protic and aprotic, polar and non-polar species, and different hydrogen-bonding capacities, covering a broad region of the Hansen solubility space [19, 20]. For each test, approximately 10 mg of film was immersed in 3 mL of the test solvent in a sealed glass vial to prevent evaporation, and the vial was kept at 45 °C for 20 days.

The three Hansen solubility parameters (dispersive, δ_D; polar, δ_P; and hydrogen-bonding, δ_H), together with the interaction radius (R_0), were estimated through numerical optimization of experimental solubility data within the Hansen space. Unlike conventional deterministic classification approaches, the present method adopts a probabilistic framework, treating solubility as a continuous phenomenon.

Experimental data, originally encoded as soluble (1), partially soluble (0.5), and insoluble (0), were reformulated as a binary response, with partially soluble systems receiving reduced statistical weight. This procedure preserves the physical continuity of the solubility transition while avoiding artificial class segmentation.

The Hansen parameters (δ_D, δ_P, δ_H, R_0) were obtained by minimizing objective functions that combine geometric consistency with probabilistic reliability using the free solubility software (https://solubility-g8rrrnnvcbchyhlc2qf5nl.streamlit.app/) [21]. In particular, multiple complementary loss functions were evaluated, including geometric penalties, log-loss, Brier score, and margin-based functions, ensuring robustness of the solution with respect to the optimization criterion. To reduce sensitivity to initialization and local minima, global and local optimization algorithms were employed, and the final parameter set was selected based on overall performance across these criteria. In this approach, polymer–solvent affinity is quantified using the Relative Energy Difference. The R_a represents the Hansen distance between the solvent and the optimized solubility center. Rather than adopting a strict threshold (RED = 1), the RED was mapped to a solubility probability using a logistic function, enabling a continuous interpretation of compatibility consistent with experimental observations near the solubility boundary [21]. Thus, solvents located near RED ≈ 1 are associated with intermediate probabilities, reflecting swelling or partial dissolution, whereas solvents far from the boundary correspond to well-defined soluble or insoluble behavior. This probabilistic reinterpretation preserves the geometric structure of Hansen space while providing a more realistic description of polymer–solvent interactions.

The methodology was applied to WPUA-0+ and WPUA-Eda(ac+) films as representative systems, enabling the evaluation of microstructural changes induced by CQDs incorporation, including shifts in the Hansen solubility center and contraction or expansion of the interaction radius. This approach allows a direct and physically interpretable assessment of how compositional modifications affect the polymer–solvent interaction landscape.

Results and discussion

Structural analysis and photoluminescent properties of CQDs

The two types of CQDs were synthesized by distinct routes, yielding materials with different photoluminescence quantum yields (QYs) and different relative surface elemental compositions. CQD-*Eda*, produced by microwave-assisted pyrolysis from citric acid (CA) and ethylenediamine (EDA), exhibited an average hydrodynamic diameter of 12.9 ± 8.2 nm and a high QY value of approximately 63% under excitation at 360 nm (Fig. 1a). CQD-*Spr*, obtained by thermal pyrolysis of Spirulina biomass, a structurally complex mixture of proteins, lipids, and carbohydrates, showed a somewhat smaller average particle size (10.9 ± 9.6 nm) but a markedly lower QY of approximately 23%. The substantial difference in QY between the two types of CQDs can be rationalized in terms of their core structures. The use of CA and EDA as precursors for CQD-*Eda* provides a controlled nitrogen-doped carbonization pathway that promotes the formation of well-defined, highly conjugated sp^2 carbon domains, which are responsible for efficient radiative recombination [13]. In contrast, Spirulina's heterogeneous composition leads to a broader distribution of fluorescent surface states and structural defects, resulting in a higher density of non-radiative recombination pathways and, consequently, a lower QY [14].

FTIR analysis confirmed that both types of CQDs bear similar surface functional groups: −OH/−NH (3406−3065 cm^{-1}, associated with the presence of water, alcohol, phenol, and amine); C−H stretching (2960 cm^{-1}, related to CH_2 and CH_3 groups); aromatic conjugated C=C (1550 cm^{-1}); C=O (1651 cm^{-1}); C=N (1629 cm^{-1}); N−H bending and C−N stretching (1520 cm^{-1}, associated with amide groups); phenolic C–OH (1270 cm^{-1}); C−O stretch of carboxylate ions (1375 cm^{-1}); C−H bending (1430 cm^{-1}); C−O single bond (1093 cm^{-1}); and aromatic C−H (904 cm^{-1}) functional groups [9, 14, 22]. The presence of carboxyl, hydroxyl, carbonyl, and nitrogen-containing groups is particularly relevant because these moieties may contribute to hydrogen bonding and polar interactions with urethane, carbonyl, and carboxylate groups of the WPUA matrix [9].

In addition to the identification of functional groups by FTIR, the X-ray photoelectron spectroscopy (XPS) surface elemental composition and zeta potential values previously reported for CQD-*Eda* [9] and CQD-*Spr* [14] are summarized in Table 2. CQD-*Eda* exhibited higher relative O and N surface contents, whereas CQD-Spr showed a predominantly carbon-rich surface, reflecting the different precursor systems and carbonization routes. The zeta potential values in water were also distinct, with CQD-*Eda* presenting a slightly negative value (− 7.21 mV) and CQD-*Spr* a positive value (+ 15.5 mV). These results show that, despite presenting similar functional groups as determined by FTIR, the two CQDs differ in their relative surface elemental composition and colloidal surface charge.

The photoluminescence properties of the CQDs were investigated by UV–vis absorption and fluorescence spectroscopy. As shown in Fig. 1c, CQD-E*da* exhibited two well-defined absorption bands at 250 and 350 nm, whereas CQD-*Spr* showed a dominant absorption peak at 250 nm accompanied by a tail extending into the visible region. In agreement with previous reports [9, 14], the absorption at 250 nm can be

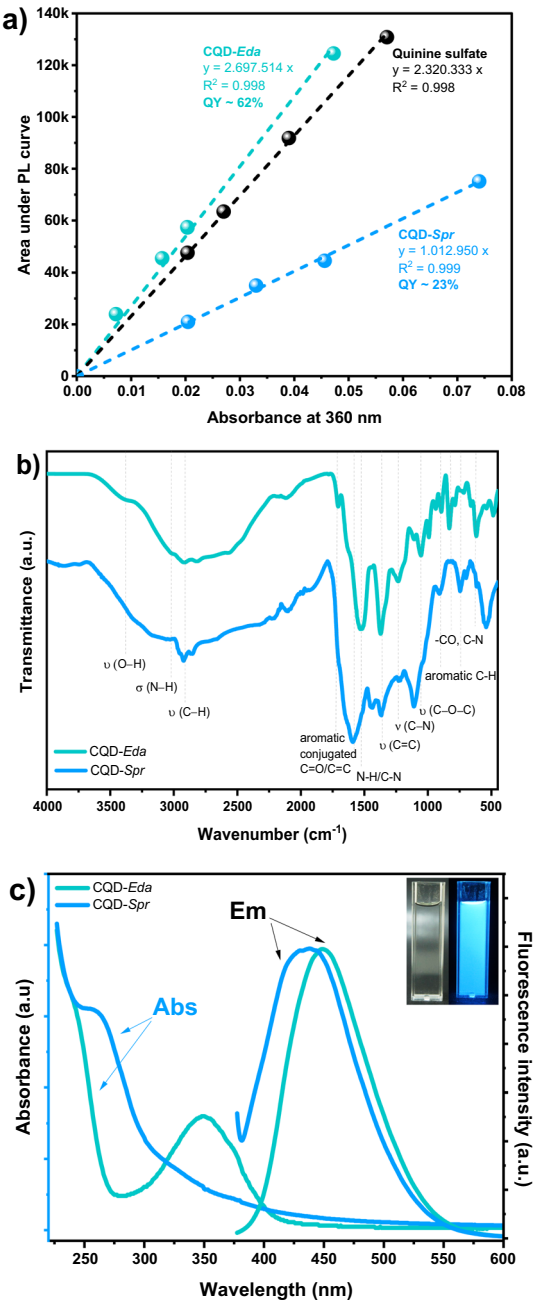


Fig. 1 (**a**) Quantum yield (QY), (**b**) FTIR spectra, and (**c**) UV–vis absorption and photoluminescence (PL) emission spectra (excitation at 360 nm) of CQD-*Eda* and CQD-*Spr*. Inset: photograph of the CQD-*Eda* aqueous solution under visible and UV irradiation

attributed to π–π* transitions of aromatic C=C domains, while the band at 350 nm, or the extended absorption tail in the case of CQD-*Spr*, is associated with n→π* transitions of C=O and C–N functional groups. These oxygen- and nitrogen-containing moieties are typically located at the CQDs surface, whereas the C=C bonds

Table 2 Surface elemental composition and zeta potential of CQD-*Eda* and CQD-*Spr*

CQD	C (%)	N (%)	O (%)	Zeta potential in water (mV)	Ref
CQD-*Eda*	39.2	17.2	43.6	− 7.2	[9]
CQD-*Spr*	67.5	9.8	22.7	+ 15.5	[14]

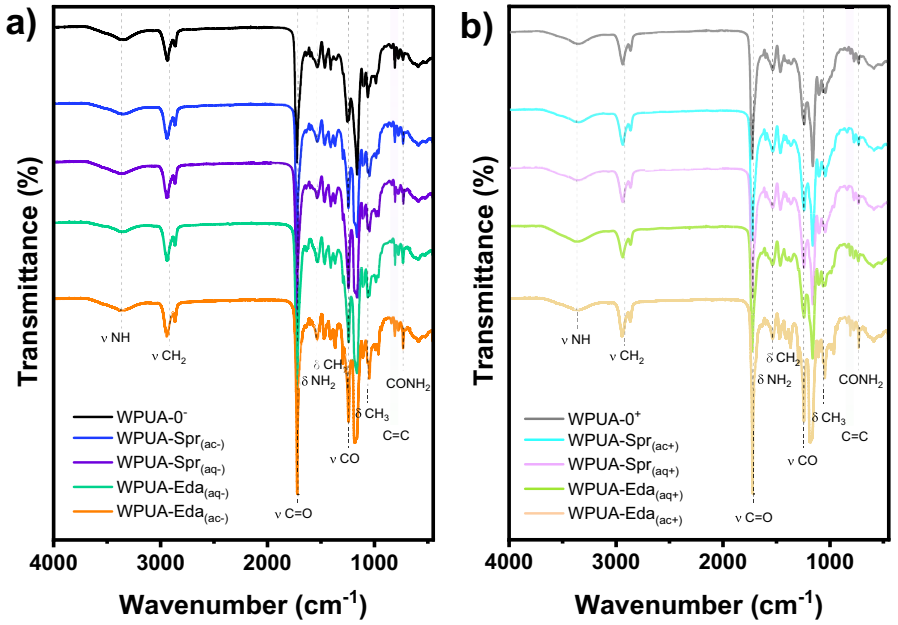


Fig. 2 FTIR spectra of the neat WPUA and WPUA/CQDs nanocomposites (**a**) before and (**b**) after UV curing

are mainly associated with the graphitic core [22]. Upon excitation at 360 nm, both CQDs exhibit a strong photoluminescence emission centered at ~450 nm. Consistently, their aqueous dispersions appeared light yellow under visible light and displayed intense blue fluorescence under UV irradiation (360 nm), as shown in the inset of Fig. 1c. Notably, the broader absorption profile of CQD-*Spr*, characterized by the extended absorption tail into the visible region rather than a discrete band at 350 nm, suggests enhanced spectral overlap with the 365 nm curing lamp. This feature indicates that CQD-*Spr* may compete more effectively with the photoinitiator across a wider wavelength range during irradiation, which is particularly relevant to the photopolymerization kinetics discussed in Sect. "Photopolymerization behavior".

Chemical structure of WPUA/CQDs nanocomposites

FTIR spectroscopy was employed to confirm the chemical structure of the films, assess structural changes induced by UV curing, and detect potential interactions between CQDs and the WPUA matrix. The spectra of both neat WPUA and WPUA/CQDs films (Fig. 2) displayed characteristic absorption bands consistent with

the expected polyurethane-acrylate architecture: 3360–3420 cm^{-1} (N–H stretching), 2955–2865 cm^{-1} (CH_2 and CH_3 stretching), 1738–1637 cm^{-1} (C=O stretching), 1525 cm^{-1} (C–N and N–H bending of urethane groups), and 1238 cm^{-1} and 1151 cm^{-1} (C–O–C asymmetric deformation) [9, 23]. The complete disappearance of the free–NCO absorption band (expected near 2270 cm^{-1}) in all films confirmed that the prepolymer synthesis was complete and that no residual isocyanate functionality was present prior to photocuring. The presence of bands at 1640 cm^{-1} (C=C stretching), 960 cm^{-1} (=CH_2 wagging), and 810 cm^{-1} (=CH out-of-plane bending) in the pre-cured films confirmed the successful incorporation of reactive acrylate C=C double bonds into the polyurethane chains [4, 24]. After UV irradiation, a pronounced reduction in the intensity and relative area of the C=C bands at 1640 and ~810 cm^{-1} was observed, reflecting consumption of C=C bonds through free-radical crosslinking [25].

No distinct new bands attributable to CQDs incorporation were resolved in the FTIR spectra of the nanocomposite films. This outcome is expected given the low CQDs loading (1.0 wt%) and the substantial spectral overlap between CQDs functional groups (hydroxyl, carboxyl, amine) and pre-existing WPUA bands. Although interfacial interactions between CQDs and the polymer matrix may occur [9], they are difficult to quantify at 1.0 wt% loading by ATR-FTIR alone.

Photopolymerization behavior

The photopolymerization kinetics of the WPUA and WPUA/CQDs systems were investigated by photo-DSC under both inert (N_2) and oxidative (O_2/air) atmospheres at a UV irradiance of 50 mW/cm^2 (Fig. 3). The polymerization profiles (Fig. 3a–d) and conversion rate curves (Fig. 3e–h) for all formulations follow the characteristic behavior of diffusion-controlled free-radical photopolymerization: an initial rapid increase in rate driven by efficient radical generation and high monomer mobility, followed by a progressive deceleration as the developing crosslinked network restricts molecular diffusion of both radicals and unreacted double bonds, which is the so-called Trommsdorff or gel effect [26, 27]. The neat UV-cured reference (WPUA-0^+) achieved maximum conversions of 92.8% (N_2) and 99.4% (O_2), with peak rates at 4.2 and 3.3 s, respectively. Although the conversion under O_2/air was slightly higher than under N_2, this apparent increase was treated cautiously and was not used as mechanistic evidence of oxygen-promoted polymerization, since molecular oxygen is known to inhibit free-radical photopolymerization by scavenging carbon-centered radicals [17].

The formulations without photoinitiator (Irgacure 2959®) were used to assess the auxiliary photoactive contribution of CQDs. WPUA-0^- showed only residual conversion under UV irradiation, reaching 6.8% under N_2 and 4.9% under O_2. In contrast, CQD-containing formulations without a photoinitiator achieved substantially higher conversions, ranging from 19.4% to 57.9% under N_2 and from 17.1% to 37.2% under O_2. These results show that CQDs contribute to photoinduced conversion even in the absence of Irgacure 2959®. However, since these conversions remained lower than those obtained with the conventional photoinitiator, CQDs are better described as

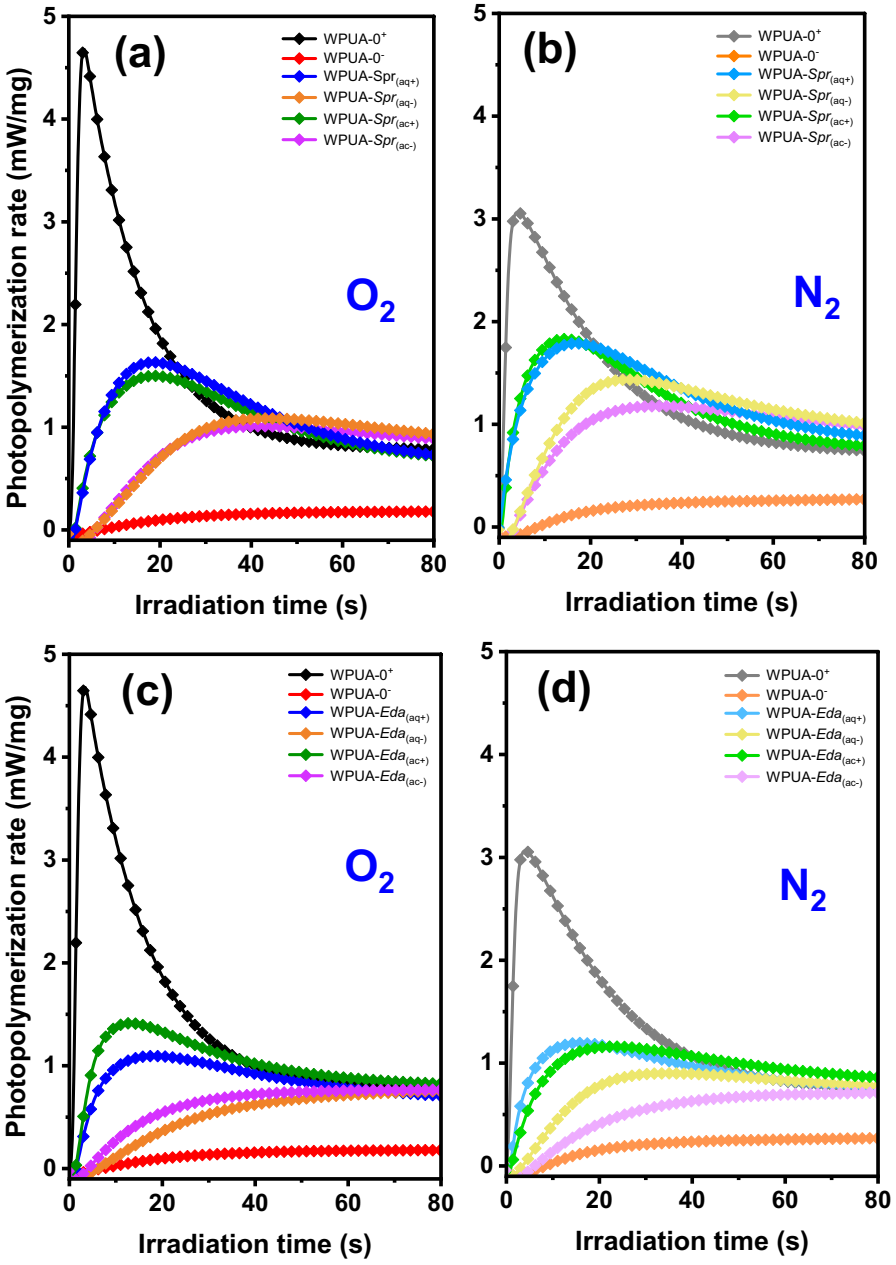


Fig. 3 (**a-d**) Photo-DSC thermograms and (**e–h**) C=C conversion (α) as a function of irradiation time for WPUA-*Spr* and WPUA-*Eda* systems under inert (N_2) and oxygen (O_2) atmospheres

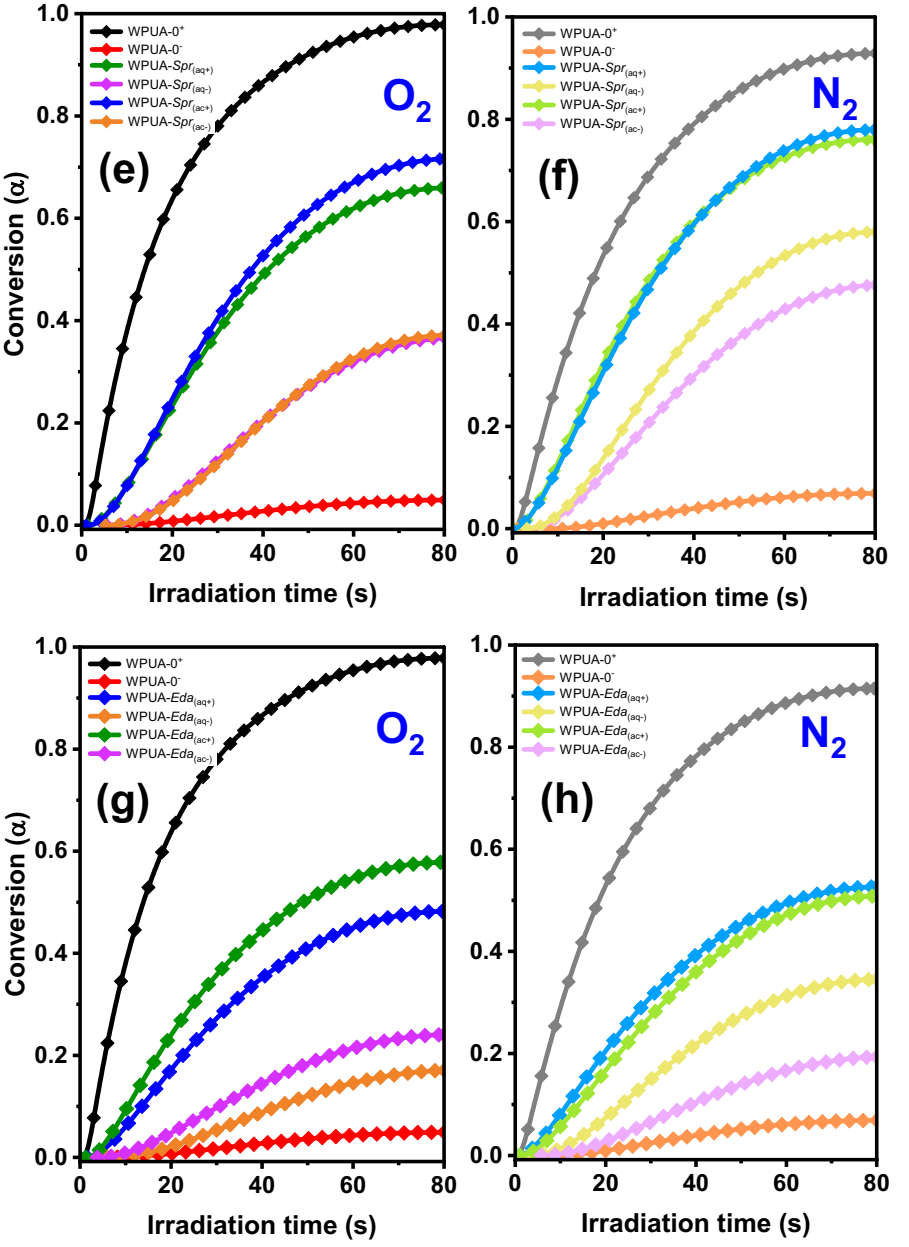


Fig. 3 (continued)

auxiliary photoactive species rather than efficient standalone photoinitiators in this WPUA system.

In the presence of a photoinitiator, all CQDs-containing formulations showed broader exothermic peaks, delayed peak maxima, and lower final conversions than WPUA-0^+ (Table 3). To separate the main contributions to curing retardation, the

Table 3 Photo-DSC curing parameters of the neat WPUA and WPUA/CQDs nanocomposites under inert (N_2) and oxygen (O_2) atmospheres (UV intensity 50 mW/cm^2)

Sample ID	N_2 atm			O_2 atm		
	ΔH (J/g)	Peak maximum (s)	α (%)	ΔH (J/g)	Peak maximum (s)	α (%)
WPUA-0^-	5.87	30.1	6.8	4.21	34.4	4.9
WPUA-0^+	79.42	4.2	92.8	85.03	3.3	99.4
WPUA-$Spr_{(aq-)}$	49.56	28.1	57.9	31.78	32.8	37.2
WPUA-$Spr_{(aq+)}$	45.01	15.6	52.6	41.26	16.9	48.3
WPUA-$Spr_{(ac-)}$	40.74	33.9	47.6	31.38	39.2	36.7
WPUA-$Spr_{(ac+)}$	65.02	13.7	76.1	56.41	17.4	65.9
WPUA-$Eda_{(aq-)}$	29.51	34.5	34.5	14.60	45.5	17.1
WPUA-$Eda_{(aq+)}$	66.65	16.5	77.9	61.32	16.8	71.7
WPUA-$Eda_{(ac-)}$	16.57	44.5	19.4	20.57	38.2	24.1
WPUA-$Eda_{(ac+)}$	43.46	22.4	50.8	49.44	12.4	57.8

Photo-DSC data were interpreted using three descriptors: the total conversion penalty, the route-dependent conversion difference, and the auxiliary CQDs photoactive contribution. The total conversion penalty under N_2 was defined as $\Delta\alpha_{total} = \alpha_{(WPUA\text{-}0^+)} - \alpha_{(WPUA\text{-}CQD^+)}$, giving 40.2 percentage points for WPUA-$Spr_{(aq+)}$, 16.7 for WPUA-$Spr_{(ac+)}$, 14.9 for WPUA-$Eda_{(aq+)}$, and 42.0 for WPUA-$Eda_{(ac+)}$. Since the CQDs type and loading were kept constant within each pair, the aqueous/acetone difference was taken as a route-dependent descriptor associated with CQDs dispersion, CQD–WPUA interfacial association, hydrogen bonding, and restricted acrylate-chain mobility. For CQD-*Spr*, acetone incorporation increased the conversion from 52.6% to 76.1% under N_2 and from 48.3% to 65.9% under O_2. Conversely, for CQD-*Eda*, acetone incorporation decreased the conversion from 77.9% to 50.8% under N_2 and reduced it under O_2, though less markedly. These opposing trends indicate that the incorporation route affects curing via CQDs-specific matrix interactions rather than solely through optical screening.

The delayed curing of CQDs-containing formulations therefore results from a balance among optical, physical, and photoactive effects. Optically, CQDs absorb part of the incident UV radiation and compete with photoinitiator for photon absorption, reducing the effective radical generation rate [12, 23]. Physically, oxygen- and nitrogen-containing groups on CQDs surfaces can interact with urethane/acrylate-rich domains through hydrogen bonding and polar interactions, increasing local microstructural constraint and reducing the mobility of acrylate-terminated chains [4, 9, 24, 26]. However, the effect is not purely inhibitory. The absence of a direct correlation between photoluminescence QY and curing behavior indicates that emission efficiency alone does not govern the Photo-DSC response. Instead, UV absorption, surface chemistry, dispersibility, interfacial association, and photoinduced charge- or energy-transfer processes must be considered together. This interpretation agrees with recent reports showing that CQDs and related carbon nanomaterials can participate in light-mediated polymerization through photoredox pathways, Type I surface-bound photoinitiating groups, and surface-mediated radical formation [28–31]. Specifically, Kütahya et al. and Luo et al. described CQDs/carbon nanomaterials as photocatalytic or photoinitiating platforms for radical polymerization [28, 29], Li et al. demonstrated Type I photoinitiation from CQDs bearing surface oxime ester groups [30],

and Lyu et al. showed quantum-dot-mediated acrylate polymerization through triplet energy transfer followed by surface-assisted radical generation [31]. Although the CQDs used here are not designed Type I photoinitiators and are not semiconductor CQDs, these studies support the broader mechanism in which nanoscale dot surfaces contribute to radical-generating photochemical pathways.

The oxygen response also fits this optical-physical-photoactive framework. Oxygen inhibition was evident in most CQDs-containing formulations, as shown by the conversion decrease of WPUA-$Spr_{(ac+)}$ from 76.1% under N_2 to 65.9% under O_2 and of WPUA-$Eda_{(aq+)}$ from 77.9% to 71.7%. In contrast, WPUA-$Eda_{(ac-)}$ and WPUA-$Eda_{(ac+)}$ showed no clear conversion decrease under O_2, suggesting an apparent attenuation of oxygen inhibition. This behavior is consistent with the photoinitiator-free controls and with the reactive oxygen species (ROS) generation previously demonstrated for WPU/CQD-*Eda* coatings, including singlet oxygen detected by 1,3-diphenylisobenzofuran (DPBF) bleaching [9]. Therefore, CQDs-mediated energy or electron transfer pathways may generate additional reactive species under oxidative conditions, partially counterbalancing oxygen inhibition without implying oxygen-promoted polymerization. Accordingly, the net curing response of WPUA/CQDs coatings reflects the competition among UV screening, incorporation-route-dependent mobility restriction, and auxiliary CQDs photoactivity, with the dominant contribution varying with CQDs surface chemistry, dispersion route, and curing atmosphere [28–31].

Thermal characterization

DSC and TGA examined the thermal behavior of neat WPUA and WPUA/CQDs films. DSC curves obtained during the second heating scan (Fig. 4a) revealed two thermal transitions in all samples: a glass transition of the soft PCL segments (T_{gSS}) near −30 °C, and a relaxation of hard-segment domains (T_{hd}) near 40 °C, consistent with the segmented microstructure of polycaprolactone-based polyurethanes [27]. No additional melting or crystallization events were detected within the analysis range. A slight increase in T_{gSS} was observed after UV curing and following CQDs incorporation, indicative of reduced segmental mobility resulting from both crosslink formation and nanoparticle–matrix interactions [9, 23]. For the hard-segment relaxation, the uncured reference (WPUA-0^-) showed a low-enthalpy endothermic transition (ΔH = 1.37 J/g, T_{hd} = 41.2 °C). UV curing increased the enthalpy of this transition (WPUA-0^+, ΔH = 2.60 J/g, T_{hd} = 40.6 °C), reflecting changes in the packing and short-range order of hard-segment domains induced by crosslinking and local structural rearrangements. The incorporation of CQD-*Spr* resulted in a modest increase in enthalpy (WPUA-$Spr_{(ac+)}$, ΔH = 2.72 J/g, T_{hd} = 40.3 °C), whereas CQD-*Eda* produced a more pronounced effect, with a substantial increase in enthalpy accompanied by a further decrease in the transition temperature (WPUA-$Eda_{(ac+)}$, ΔH = 6.85 J/g, T_{hd} = 38.8 °C). These results suggest that CQD-*Eda* interacts strongly with the hard-segment domains, possibly through hydrogen bonding between CQDs carboxyl/amine groups and urethane carbonyl or N–H moieties [9].

TGA results (Fig. 4b) revealed a three-stage degradation pattern characteristic of segmented PCL-based polyurethanes [32]: (i) decomposition of urethane bonds in

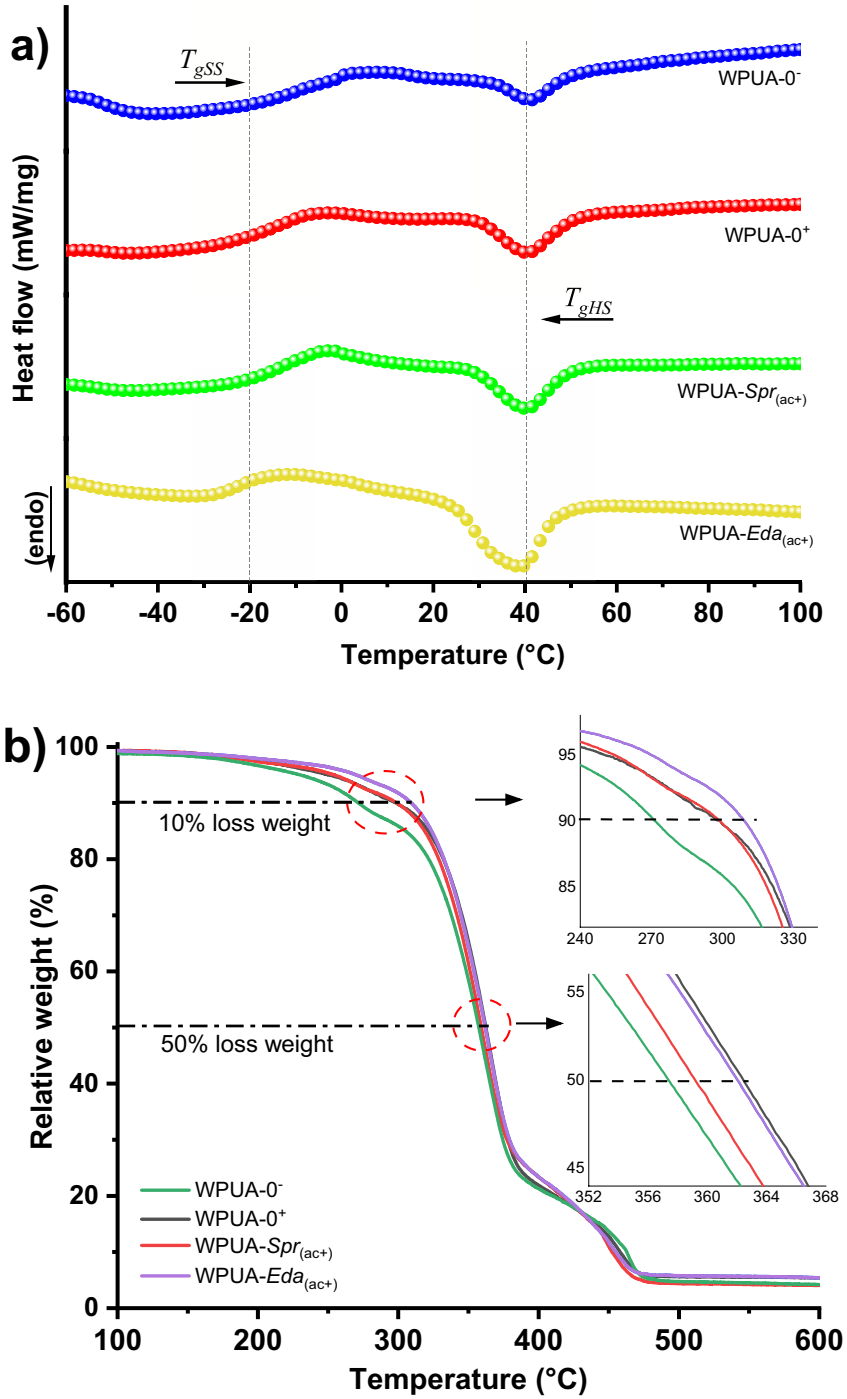


Fig. 4 (**a**) DSC and (**b**) TGA curves of cured neat WPUA and WPUA/CQDs nanocomposites

rigid segments (250–380 °C); (ii) degradation of soft segments, crosslinked domains, and residual ester groups (380–480 °C); and (iii) decomposition of carbonaceous residues and CQDs-derived thermally stable structures above 480 °C [32]. The temperature at 10% weight loss ($T_{10\%}$) increased from 270.9 °C for the uncured material (WPUA-0^{-}) to 298.2 °C after UV curing (WPUA-0^{+}), consistent with the well-established correlation between crosslink density and thermal stability in acrylate networks [33]. Incorporation of 1.0 wt.% of CQD-*Eda* acetone-dispersed (WPUA-$Eda_{(ac+)}$) further increased $T_{10\%}$ to 309.1 °C, an improvement of ~11 °C relative to the neat UV-cured film. This enhancement can be attributed to hydrogen bonding and polar interactions between CQDs surface groups and the WPUA chains, which restrict backbone mobility and increase the activation energy for bond scission [23]. In contrast, WPUA-$Spr_{(ac+)}$ showed a less pronounced improvement, reflecting its weaker interfacial integration, as evidenced by its smaller effects on curing kinetics and DSC transitions. Interestingly, when water-dispersed CQDs were incorporated during the phase inversion process, the resulting films exhibited a lower onset decomposition temperature than those prepared with CQDs dispersed in acetone. This behavior can be attributed to differences in interfacial interactions and crosslinking density within the polymer network [23]. However, the temperatures at 50% weight loss are comparable across all samples, indicating that the overall thermal stability is not significantly affected. Instead, the presence of CQDs appears to enhance stability primarily during the initial stages of degradation, in agreement with the DSC results [34].

Physical–mechanical properties

The mechanical properties, hardness, gel content, and water absorption of all films are summarized in Table 4. UV curing produced a dramatic transformation in the mechanical behavior of the neat WPUA: hardness increased from 56.1 ± 0.8 Shore A (WPUA-0^{-}) to 80.8 ± 1.9 Shore A (WPUA-0^{+}), tensile strength from 2.9 ± 0.6 to 4.3 ± 0.3 MPa, while elongation at break decreased sharply from 451.4 ± 60.1% to 41.9 ± 2.3%. This stiffening is a direct consequence of the formation of a densely crosslinked acrylate network [27], as confirmed by the high gel content (97.8%) and the reduction in water absorption from 33.9% to 16.1%.

CQDs-containing UV-cured films showed lower gel content than WPUA-0^{+} (83–93%), consistent with the reduced conversion measured by Photo-DSC, indicating partial inhibition of acrylate crosslinking [8]. Despite this lower covalent crosslink density, CQDs-containing formulations showed higher hardness and, in some cases, higher tensile strength than WPUA-0^{+}. Shore A hardness reached 94.1 ± 1.3 for WPUA-Spr(ac^{+}) and 94.0 ± 3.1 for WPUA-Eda(ac^{+}), while tensile strengths of 6.6 ± 1.4 and 6.1 ± 1.2 MPa were achieved, respectively. This improvement in mechanical properties, despite lower gel content, can be explained by the contribution of physical nanoparticle–matrix interactions (hydrogen bonding, polar coupling) to the network's overall load-bearing capacity [4, 9]. The reinforcement was more pronounced for acetone-dispersed CQDs than for water-dispersed CQDs, directly reflecting the tighter polymer–nanoparticle integration achieved by the former route [9, 32].

Water absorption values for CQDs-containing films (30.6–37.6%) were higher than that of WPUA-0^{+} (16.1%), which can be attributed to the hydrophilic surface

Table 4 Physical–mechanical properties of the neat WPUA and WPUA/CQDs nanocomposites

Sample ID	Hardness (Shore A)	Tensile strength (MPa)	Elongation at break (%)	Gel content (%)	Water absorption (%)
WPUA-0^{-}	56.1 ± 0.8^{e}	2.9 ± 0.6^{cde}	451.4 ± 60.1^{b}	77.5 ± 0.1^{g}	33.9 ± 2.5^{a}
WPUA-0^{+}	80.8 ± 1.9^{c}	4.3 ± 0.3^{bc}	41.9 ± 2.3^{d}	97.8 ± 0.6^{a}	16.1 ± 0.8^{b}
WPUA-$Spr_{(aq-)}$	57.2 ± 1.0^{de}	2.1 ± 0.8^{de}	348.9 ± 45.2^{c}	92.6 ± 0.1^{b}	37.6 ± 3.0^{a}
WPUA-$Spr_{(aq+)}$	92.0 ± 2.0^{ab}	5.1 ± 1.7^{ab}	50.4 ± 4.8^{d}	85.6 ± 0.7^{e}	33.7 ± 2.6^{a}
WPUA-$Spr_{(ac-)}$	55.5 ± 2.1^{e}	3.2 ± 0.6^{cd}	570.2 ± 32.9^{a}	88.2 ± 0.4^{d}	34.4 ± 3.1^{a}
WPUA-$Spr_{(ac+)}$	94.1 ± 1.3^{a}	6.6 ± 1.4^{a}	34.8 ± 5.9^{d}	83.2 ± 0.4^{f}	33.7 ± 2.8^{a}
WPUA-$Eda_{(aq-)}$	49.5 ± 0.7^{f}	2.9 ± 0.2^{cde}	427.7 ± 8.6^{b}	89.5 ± 0.3^{c}	36.4 ± 0.9^{a}
WPUA-$Eda_{(aq+)}$	90.3 ± 1.0^{b}	5.4 ± 0.4^{ab}	44.7 ± 9.7^{d}	92.5 ± 0.5^{b}	35.2 ± 2.3^{a}
WPUA-$Eda_{(ac-)}$	60.5 ± 1.3^{d}	1.1 ± 0.1^{e}	45.8 ± 8.1^{d}	85.4 ± 0.4^{e}	33.4 ± 8.7^{a}
WPUA-$Eda_{(ac+)}$	94.0 ± 3.1^{a}	6.1 ± 1.2^{ab}	32.6 ± 2.4^{d}	83.2 ± 0.6^{f}	30.6 ± 4.8^{a}

Values are expressed as mean ± standard deviation. Within each column, values sharing at least one common superscript letter are not statistically different according to Tukey's test ($p < 0.05$), whereas values with no common letters are statistically different

groups of CQDs that increase the affinity of the network for water. Although some acetone-incorporated CQDs films showed numerically lower water absorption than their aqueous-dispersion counterparts, these differences were not statistically significant among the CQDs-containing formulations. Therefore, the water absorption results indicate that CQDs incorporation increases the hydrophilic character of the films, whereas the effect of the incorporation route on water uptake should be interpreted as a tendency rather than a statistically confirmed difference.

Surface free energy

Surface free energy values determined by the Owens–Wendt method are presented in Table 5. The non-cured WPUA-0^{-} exhibited a relatively high surface energy (γ_S = 38.3 mN/m) dominated by its polar component (γ_S^P = 24.3 mN/m), attributable to the hydrophilic ionic groups (carboxylate and urethane moieties) concentrated at the film surface [9]. After UV curing (WPUA-0^{+}), the total surface energy decreased modestly to 35.8 mN/m, with a slight increase in the polar component (γ_S^P = 25.3 mN/m) and a decrease in the dispersive component (γ_S^D = 10.5 mN/m). This change reflects the increased crosslink density following photopolymerization of PETA, which restricts the surface mobility of hydrophilic groups and promotes a slightly more hydrophobic character [5, 35].

Incorporation of CQDs produced only minor changes in surface free energy: WPUA-*Spr*$_{(ac^+)}$ and WPUA-*Eda*$_{(ac^+)}$ exhibited values of 36.3 and 36.4 mN/m, respectively, comparable to WPUA-0^{+}. This finding is consistent with the inherently shallow sampling depth of contact angle measurements (~1–2 nm), which reflects predominantly the chemistry of the outermost film surface rather than the bulk. The persistently higher polar contribution ($\gamma_S^P > \gamma_S^D$) in all samples confirms that polar interactions dominate the surface behavior of these materials regardless of CQDs incorporation [33, 36]. The differences in swelling behavior observed among formulations (Table 4) are therefore more likely to be related to changes in the internal network microstructure and hydrophilicity than to variations in surface polarity [23].

Table 5 Contact angle (θ) and surface free energy (γ_S) of the neat WPUA and WPUA/CQDs nanocomposites, with their respective dispersive (γ_S^D) and polar (γ_S^P) contributions

Sample ID	Contact angle (θ, °C)				Surface free energy (mN/m)			R^2
	Water	Diethylene glycol	Dimethyl sulfoxide	Hexadecane	γ_S	γ_S^D	γ_S^P	
WPUA-0^{-}	68.4 ± 0.8	30.8 ± 0.7	36.5 ± 1.8	25.0 ± 0.4	38.3	13.9	24.3	0.987
WPUA-0^{+}	73.4 ± 1.2	38.9 ± 0.9	37.8 ± 1.7	20.0 ± 1.1	35.8	10.5	25.3	0.970
WPUA-*Spr*$_{(ac+)}$	71.2 ± 1.1	40.0 ± 1.3	39.3 ± 0.6	19.1 ± 0.9	36.3	11.9	24.4	0.978
WPUA-*Eda*$_{(ac+)}$	70.1 ± 1.8	40.7 ± 0.8	41.3 ± 0.8	19.2 ± 0.7	36.4	12.6	23.7	0.991

Solubility parameters using optimized RED approach

The solubility behavior of WPUA-0^{+} and WPUA-$Eda_{(ac+)}$ films was evaluated using Hansen solubility parameters (δ_D, δ_P, δ_H) and the interaction radius (R_0) obtained through numerical optimization. The experimental response included insoluble (0), partially soluble (0.5), and soluble (1) systems, enabling the identification of a transition region between compatible and incompatible solvents. The Relative Energy Difference (RED = Ra/R₀) was used as a continuous descriptor of polymer–solvent affinity, highlighting gradual changes in compatibility rather than a sharp boundary, in accordance with recent probabilistic interpretations of the RED criterion in Hansen solubility theory [21]. Compared to WPUA-0^{+}, the WPUA-$Eda_{(ac+)}$ system exhibits a reduced number of fully compatible solvents and a higher concentration of borderline (0.5) responses, indicating a more selective and restrictive solubility domain after CQDs incorporation. The evaluated solvents and corresponding classifications are summarized in Table 6.

The estimated HSP values for the neat WPUA-0^{+} were δ_D = 20.68, δ_P = 10.73, δ_H = 9.29 $MPa^{1/2}$, with an interaction radius R_0 = 12.46 $MPa^{1/2}$. These values are consistent with those reported for polycaprolactone-based polyurethanes [9, 38, 39], supporting the reliability of the fitting procedure. Upon incorporation of CQD-*Eda* (WPUA-$Eda_{(ac^{+})}$), a subtle but systematic redistribution of the HSP components was observed: δ_D increased to 20.90 $MPa^{1/2}$, whereas δ_P and δ_H decreased to 9.03 and 7.64 $MPa^{1/2}$, respectively. The increase in δ_D reflects the contribution of the aromatic sp^2-carbon domains of the CQDs core to dispersive van der Waals interactions within the network. Simultaneously, the decrease in δ_H indicates a lower contribution from hydrogen-bonding interactions. The decrease in δ_P suggests that polar CQDs surface groups are sequestered through interfacial hydrogen bonding with the matrix rather than contributing as free polar entities [9]. This suggests that incorporating CQDs modifies intermolecular interactions within the polymer matrix without significantly altering its overall hydrogen-bonding capability.

The most significant finding is the contraction of the interaction radius from R_0 = 12.46 to 8.44 $MPa^{1/2}$, corresponding to a narrowing of the solubility sphere (Fig. 5). This reduced R_0 indicates that WPUA-$Eda_{(ac^{+})}$ is compatible with a more restricted range of solvents, reflecting a more constrained and rigid polymer network. This behavior is entirely consistent with the mechanical, thermal, and Photo-DSC results: CQDs incorporation reduced chain mobility, increased network rigidity, and thereby restricted solvent accessibility. Analogous reductions in solubility sphere size upon structural modifications have been reported in thermoplastic polyurethane systems [38, 39]. The narrowing of the solubility sphere also has practical implications for coating formulation: it means that WPUA-$Eda_{(ac^{+})}$ films would exhibit better resistance to a broader range of industrial solvents than neat UV-cured WPUA, an attribute of considerable relevance for protective coating applications.

Principal component analysis (PCA) was applied to correlate curing behavior and final properties of the WPUA/CQDs systems using conversion, peak time, gel content, and tensile strength as variables. PC1 and PC2 explained 78.7% and 15.8% of the total variance, respectively, for a total of 94.5%, indicating that the system's main trends are well represented in two dimensions. The remaining variance (PC3 and

Table 6 Suitable and non-suitable solvents in solubility tests and their solubility parameters [19, 37]

	Solvent	Solubility parameters ($MPa^{1/2}$)				
		δ_D	δ_P	δ_H	WPUA-0^+	WPUA-$Eda_{(ac+)}$
1	Diethyl ether	14.5	2.9	5.1	0	0
2	Hexane	14.9	0.0	0.0	0	0
3	Diethylamine	14.9	2.3	6.1	0	0
4	Methanol	15.1	12.3	22.3	0.5	0
5	Acetonitrile	15.3	18.0	6.1	0	0
6	Triethylamine	15.5	0.4	1.0	0	0
7	Acetone	15.5	10.4	7.0	0.5	0
8	Propan-2-ol	15.8	6.1	16.4	0	0
9	Ethanol	15.8	8.8	19.4	0	0
10	Methyl ethyl ketone	16.0	9.0	5.1	1	0
11	N-dibutylamine	16.2	4.5	8.0	0	0
12	Hexadecane	16.3	0.0	0.0	0	0
13	Diethylene glycol	16.6	12.0	20.7	1	0
14	Cyclohexane	16.8	0.0	0.2	0	0
15	Tetrahydrofuran	16.8	5.7	8.0	1	0
16	1,2-Propanediol	16.8	9.4	23.3	0	0
17	Glycerol/ethanol 60/40	16.8	10.8	25.3	0	0
18	Octan-1-ol	17.0	3.3	11.9	0	0
19	Diethylene glycol/m-cresol 70/30	17.0	9.9	18.4	1	0
20	Triethanolamine	17.3	22.4	23.3	0	0
21	Glycerol	17.4	12.1	29.3	0	0
22	N,N-dimethylformamide	17.4	13.7	11.3	1	1
23	Xylene	17.8	1.0	3.1	1	0
24	Chloroform	17.8	3.1	5.7	0.5	0.5
25	DMSO/ethanol 80/20	17.9	14.9	12.0	1	0
26	Toluene	18.0	1.4	2.0	1	0
27	m-Cresol	18.0	5.1	12.9	1	1
28	Water	18.1	12.9	15.5	0.5	0.5
29	Dichloromethane	18.2	6.3	6.1	1	1
30	Benzyl alcohol	18.4	6.3	13.7	0.5	0.5
31	Dimethyl sulfoxide	18.4	16.4	10.2	1	0
32	Dioxane	19.0	1.8	7.4	1	1
33	Chlorobenzene	19.0	4.3	2.0	1	1
34	Pyridine	19.0	8.8	5.9	1	1

The Relative Energy Difference (RED) was calculated from optimized Hansen solubility parameters. Instead of using a strict RED = 1 threshold, RED was treated as a continuous measure of interaction, and solubility was encoded probabilistically (0 = insoluble, 0.5 = partially soluble, and 1 = soluble), with partially soluble systems accounted for through weighted contributions

PC4, <6%) is associated with minor effects and was not considered for interpretation. PC1 is mainly related to curing efficiency, with positive contributions from conversion and gel content and a negative contribution from peak time. PC2 is primarily associated with tensile strength, reflecting the mechanical performance of the cured networks and indicating that mechanical properties are not directly coupled with curing efficiency.

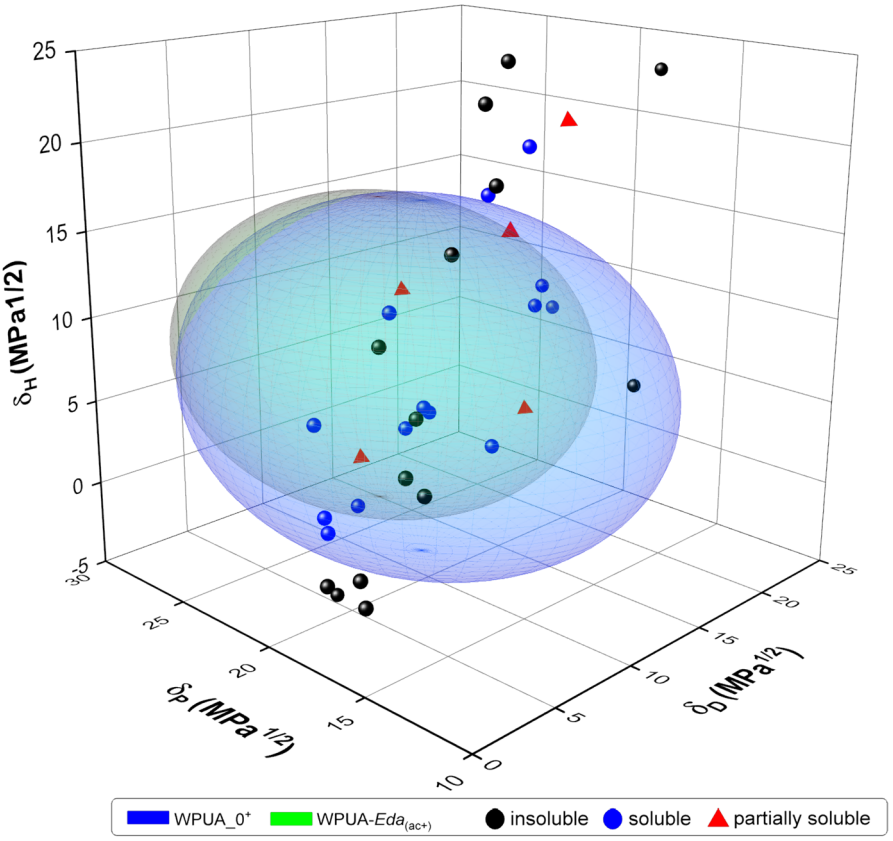


Fig. 5 Hansen solubility sphere calculated from the HSPs and R_0 values for WPUA-0^+ (blue sphere) and WPUA-$Eda_{(ac+)}$ (green sphere). Blue circles, black circles, and red triangles represent soluble, insoluble, and partially soluble solvents, respectively, as listed in Table 6

As shown in Fig. 6, the neat WPUA system is positioned at high PC1 values, indicating higher conversion and gel content. The WPUA-$Spr_{(ac+)}$ sample is shifted along PC2, indicating improved tensile strength, while WPUA-$Spr_{(aq+)}$ appears at negative PC2 values, suggesting lower mechanical performance. The Eda-modified systems exhibit intermediate behavior, with WPUA-$Eda_{(aq+)}$ located near the origin and WPUA-$Eda_{(ac+)}$ shifted towards lower PC1 values, indicating reduced curing efficiency. The PCA reveals that curing behavior and mechanical performance are partially decoupled, with the final properties being influenced by both curing kinetics and CQDs–matrix interactions.

Conclusion

This study demonstrated that CQDs act as multifunctional modifiers in UV-curable WPUA coatings, affecting curing kinetics and final properties. The incorporation of CQDs reduced the C=C conversion from 92.8% (WPUA-0^+) to 50.8%–77.9%

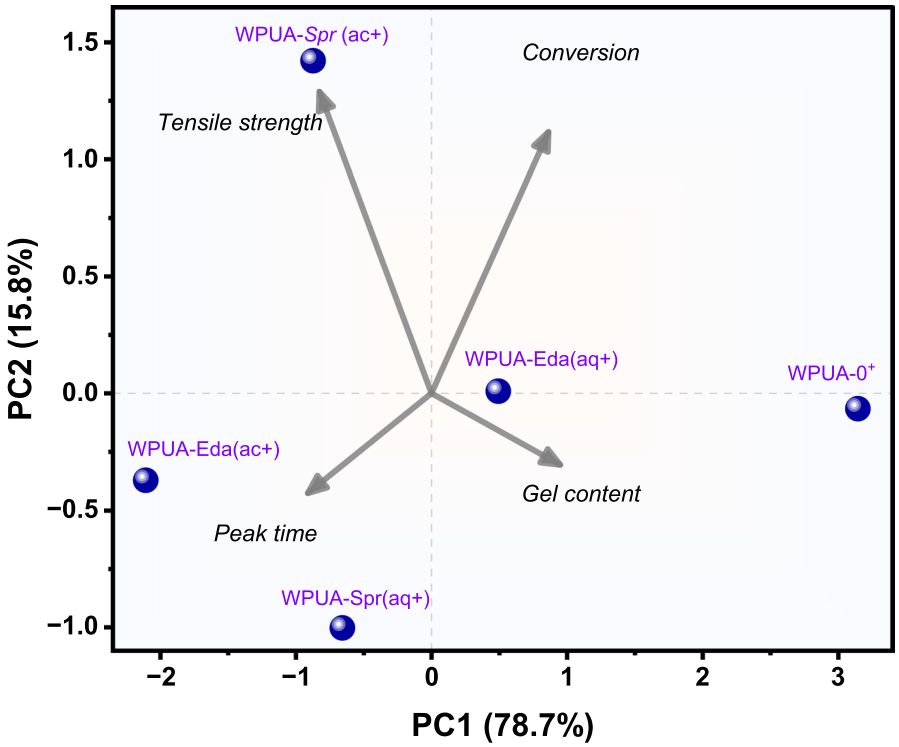


Fig. 6 Principal component analysis (PCA) biplot of WPUA/CQDs systems based on conversion, peak time, gel content, and tensile strength. The first two principal components (PC1 and PC2) account for 78.7% and 15.8% of the total variance, respectively

(≈16–45% reduction), while increasing the peak time from 4.2 s to 13.7–22.4 s (≈3–5× longer), indicating curing retardation caused by competitive UV absorption and route-dependent mobility restrictions. However, photoinitiator-free controls showed that CQDs are not merely passive UV filters, but auxiliary photoactive modifiers under irradiation. Despite lower degrees of conversion and gel content (97.8% → 83–93%), CQDs-containing systems exhibited improved mechanical and thermal performance. Tensile strength increased from 4.3 MPa (WPUA-0^{+}) to 6.1–6.6 MPa (≈40–53% increase), and thermal stability ($T_{10\%}$) increased from 298.2 °C to 309.1 °C (≈+11 °C). These results highlight the dominant role of nanoparticle–matrix interactions in reinforcing the network, compensating for reduced covalent crosslinking. The comparison between CQDs types revealed that differences in photoluminescence quantum yield (≈23% vs ≈62%) had only a minor impact on curing behavior, confirming that surface chemistry, rather than optical emission, governs the system's response. In addition, the incorporation route strongly influenced performance, with acetone-dispersed CQDs leading to more pronounced kinetic effects and superior mechanical reinforcement. CQDs incorporation introduces a trade-off between curing efficiency and performance, which can be strategically tuned through nanoparticle surface functionality and processing route. These findings provide prac-

tical guidelines for designing CQDs-modified UV-curable coatings with enhanced mechanical and thermal properties.

Acknowledgements This study was financed in part by the Coordenação de Aperfeiçoamento de Pessoal de Nível Superior—Brasil (CAPES)—Finance Code 001. CNPq – National Council for Scientific and Technological Development, Brazil (402505/2025-5, 306041/2024-3, 307914/2023-2 and 150611/2025-0) and FAPERGS – Fundação de Amparo a Pesquisa do Estado do Rio Grande do Sul (PqG-2023-24/2551-0001483-7) also supported this work.

Author contribution L.D.A. conceived the study, performed the investigation, methodology, data curation, formal analysis, and wrote the original draft. M.G.M.B. and G.S.C. reviewed the manuscript. F.T.G.D. contributed to writing and reviewing the manuscript. M.S. reviewed the manuscript. O.B. supervised the work and reviewed the manuscript. All authors read and approved the final manuscript.

Data availability Research data supporting the findings of this study are included within the article. Additional data are available from the corresponding author upon reasonable request.

Declarations

Conflicts of interest The authors have no conflicts of interest to declare.

Open Access This article is licensed under a Creative Commons Attribution 4.0 International License, which permits use, sharing, adaptation, distribution and reproduction in any medium or format, as long as you give appropriate credit to the original author(s) and the source, provide a link to the Creative Commons licence, and indicate if changes were made. The images or other third party material in this article are included in the article's Creative Commons licence, unless indicated otherwise in a credit line to the material. If material is not included in the article's Creative Commons licence and your intended use is not permitted by statutory regulation or exceeds the permitted use, you will need to obtain permission directly from the copyright holder. To view a copy of this licence, visit http://creativecommons.org/licenses/by/4.0/.

References

1. Dall Agnol L, Dias FTG, Ornaghi HL, Sangermano M, Bianchi O (2021) UV-curable waterborne polyurethane coatings: a state-of-the-art and recent advances review. Prog Org Coat 154:106156. https://doi.org/10.1016/j.porgcoat.2021.106156
2. Decker C (2003) Kinetic study and new applications of UV radiation curing. Macromol Rapid Commun 23(18):1067–1093. https://doi.org/10.1002/marc.200290014
3. Etxaniz I, Llorente O, Aizpurua J, Martín L, González A, Irusta L (2018) Dispersion characteristics and curing behaviour of waterborne UV crosslinkable polyurethanes based on renewable dimer fatty acid polyesters. J Polym Environ 27(1):189–197. https://doi.org/10.1007/s10924-018-1334-0
4. Zhang T, Wu W, Wang X, Mu Y (2010) Effect of average functionality on properties of UV-curable waterborne polyurethane-acrylate. Prog Org Coat 68(3):201–207. https://doi.org/10.1016/j.porgcoat.2010.02.004
5. Li K, Shen Y, Fei G, Wang H, Wang C (2014) The effect of PETA/PETTA composite system on the performance of UV curable waterborne polyurethane acrylate. J Appl Polym Sci 132(2):41262. https://doi.org/10.1002/app.41262
6. Feng J, Ye D (2019) Self-photoinitiating water-diluted polyurethane acrylates and their UV-curing kinetics. Prog Org Coat 129:300–308. https://doi.org/10.1016/j.porgcoat.2019.01.027
7. Bai CY, Zhang XY, Dai JB, Li WH (2006) A new UV curable waterborne polyurethane: effect of C=C content on the film properties. Prog Org Coat 55(3):291–295. https://doi.org/10.1016/j.porgcoat.2005.12.002

8. Feng J, Ye D (2019) Polymerizable ZnO photoinitiators of surface modification with hydroxyl acrylates and photopolymerization with UV-curable waterborne polyurethane acrylates. Eur Polym J 120:109252. https://doi.org/10.1016/j.eurpolymj.2019.109252
9. Dall Agnol L, Dias FTG, Bianchi O (2023) Photoactive coating based on waterborne polyurethane and carbon quantum dots as a prevention strategy for bacterial resistance. Prog Org Coat 179:107492. https://doi.org/10.1016/j.porgcoat.2023.107492
10. Hwang H-D, Park C-H, Moon J-I, Kim H-J, Masubuchi T (2011) UV-curing behavior and physical properties of waterborne UV-curable polycarbonate-based polyurethane dispersion. Prog Org Coat 72(4):663–675. https://doi.org/10.1016/j.porgcoat.2011.07.009
11. Yim YJ, Yoon YH, Kim SH, Lee JH, Chung DC, Kim BJ (2025) Carbon nanotube/polymer composites for functional applications. Polymers (Basel) 17(1):119. https://doi.org/10.3390/polym17010119
12. Ingrosso C, Esposito Corcione C, Striani R, Comparelli R, Striccoli M, Agostiano A, Curri ML, Frigione M (2015) UV-curable nanocomposite based on methacrylic-siloxane resin and surface-modified TiO2 nanocrystals. ACS Appl Mater Interfaces 7(28):15494–15505. https://doi.org/10.1021/acsami.5b03731
13. Wang B, Lu S (2022) The light of carbon dots: from mechanism to applications. Matter 5(1):110–149. https://doi.org/10.1016/j.matt.2021.10.016
14. Dall Agnol L, Neves RM, Maraschin M, Moura S, Ornaghi HL, Dias FTG, Bianchi O (2021) Green synthesis of Spirulina-based carbon dots for stimulating agricultural plant growth. Sustain Mater Technol 30:e00347. https://doi.org/10.1016/j.susmat.2021.e00347
15. Niu K-K, Ma C-Q, Dong R-Z, Liu H, Yu S-S, Xing L-B (2024) Nitrogen-doped carbon dots as photocatalysts for organic synthesis: effect of nitrogen content on catalytic activity. Nano Res 17(6):4825–4833. https://doi.org/10.1007/s12274-024-6451-6
16. Peruzzo PJ, Anbinder PS, Pardini FM, Pardini OR, Plivelic TS, Amalvy JI (2016) On the strategies for incorporating nanosilica aqueous dispersion in the synthesis of waterborne polyurethane/silica nanocomposites: effects on morphology and properties. Mater Today Commun 6:81–91. https://doi.org/10.1016/j.mtcomm.2016.01.002
17. Ligon SC, Husar B, Wutzel H, Holman R, Liska R (2014) Strategies to reduce oxygen inhibition in photoinduced polymerization. Chem Rev 114(1):557–589. https://doi.org/10.1021/cr3005197
18. Owens DK, Wendt RC (2003) Estimation of the surface free energy of polymers. J Appl Polym Sci 13(8):1741–1747. https://doi.org/10.1002/app.1969.070130815
19. Gharagheizi F (2006) New procedure to calculate the Hansen solubility parameters of polymers. J Appl Polym Sci 103(1):31–36. https://doi.org/10.1002/app.23874
20. Pereira CN, Paim L, da Cruz JA, Agnol LD, Mauler RS, Bianchi O (2024) Determination of carbon nanoparticle dispersion solubility parameters using the classic Hansen and the DiPEVa method. J Mol Liq 393:123540. https://doi.org/10.1016/j.molliq.2023.123540
21. Bianchi O (2026) A probabilistic interpretation of the relative energy difference in Hansen solubility theory. Macromol Theory Simul 35:e70045. https://doi.org/10.1002/mats.70045
22. Choi YK, Choi TR, Gurav R, Bhatia SK, Park YL, Kim HJ, Kan E, Yang YH (2020) Adsorption behavior of tetracycline onto *Spirulina* sp. (microalgae)-derived biochars produced at different temperatures. Sci Total Environ 710:136282. https://doi.org/10.1016/j.scitotenv.2019.136282
23. Li K, Shen Y, Fei G, Wang H, Li J (2015) Preparation and properties of castor oil/pentaerythritol triacrylate-based UV curable waterborne polyurethane acrylate. Prog Org Coat 78:146–154. https://doi.org/10.1016/j.porgcoat.2014.09.012
24. Llorente O, Fernández-Berridi MJ, González A, Irusta L (2016) Study of the crosslinking process of waterborne UV curable polyurethane acrylates. Prog Org Coat 99:437–442. https://doi.org/10.1016/j.porgcoat.2016.06.020
25. Lee TJ, Kwon SH, Kim BK (2014) Biodegradable sol–gel coatings of waterborne polyurethane/gelatin chemical hybrids. Prog Org Coat 77(6):1111–1116. https://doi.org/10.1016/j.porgcoat.2014.03.011
26. Sow C, Riedl B, Blanchet P (2010) Kinetic studies of UV-waterborne nanocomposite formulations with nanoalumina and nanosilica. Prog Org Coat 67(2):188–194. https://doi.org/10.1016/j.porgcoat.2009.10.002
27. Xu J, Jiang Y, Zhang T, Dai Y, Yang D, Qiu F, Yu Z, Yang P (2018) Synthesis of UV-curing waterborne polyurethane-acrylate coating and its photopolymerization kinetics using FT-IR and photo-DSC methods. Prog Org Coat 122:10–18. https://doi.org/10.1016/j.porgcoat.2018.05.008

28. Kutahya C, Zhai Y, Li S, Liu S, Li J, Strehmel V, Chen Z, Strehmel B (2021) Distinct sustainable carbon nanodots enable free radical photopolymerization, photo-ATRP and photo-CuAAC chemistry. Angew Chem Int Ed Engl 60:10983–10991. https://doi.org/10.1002/anie.202015677
29. Luo X, Zhai Y, Wang P, Tian B, Liu S, Li J, Yang C, Strehmel V, Li S, Matyjaszewski K, Yilmaz G, Strehmel B, Chen Z (2024) Light-mediated polymerization catalyzed by carbon nanomaterials. Angew Chem Int Ed Engl 63:e202316431. https://doi.org/10.1002/anie.202316431
30. Li R, Guo H, Luo X, Wang Q, Pang Y, Li S, Liu S, Li J, Strehmel B, Chen Z (2024) Type I photoinitiator based on sustainable carbon dots. Angew Chem Int Ed Engl 63:e202404454. https://doi.org/10.1002/anie.202404454
31. Lyu Y, Nie H, Du J, Wu K (2025) Quantum dots enabling all-in-one controllable polymerization through triplet energy transfer. Nat Commun 16:10013. https://doi.org/10.1038/s41467-025-64994-8
32. Ornaghi HL, Monticeli FM, Neves RM, Agnol LD, Bianchi O (2023) Use of a response surface methodology to model thermal decomposition behavior of polyurethane. Polym Bull (Berl) 81(1):391–402. https://doi.org/10.1007/s00289-023-04706-8
33. Xu J, Rong X, Chi T, Wang M, Wang Y, Yang D, Qiu F (2013) Preparation, characterization of UV-curable waterborne polyurethane-acrylate and the application in metal iron surface protection. J Appl Polym Sci 130(5):3142–3152. https://doi.org/10.1002/app.39539
34. Li C, Xiao H, Wang X, Zhao T (2018) Development of green waterborne UV-curable vegetable oil-based urethane acrylate pigment prints adhesive: preparation and application. J Clean Prod 180:272–279. https://doi.org/10.1016/j.jclepro.2018.01.193
35. Hwang HD, Kim HJ (2011) UV-curable low surface energy fluorinated polycarbonate-based polyurethane dispersion. J Colloid Interface Sci 362(2):274–284. https://doi.org/10.1016/j.jcis.2011.06.044
36. Mishra V, Desai J, Patel KI (2018) (UV/Oxidative) dual curing polyurethane dispersion from cardanol based polyol: synthesis and characterization. Ind Crops Prod 111:165–178. https://doi.org/10.1016/j.indcrop.2017.10.015
37. Zuaznabar-Gardona JC, Fragoso A (2019) Determination of the Hansen solubility parameters of carbon nano-onions and prediction of their dispersibility in organic solvents. J Mol Liq 294:111646. https://doi.org/10.1016/j.molliq.2019.111646
38. Gallu R, Méchin F, Dalmas F, Gérard J-F, Perrin R, Loup F (2020) On the use of solubility parameters to investigate phase separation-morphology-mechanical behavior relationships of TPU. Polymer 207:122882. https://doi.org/10.1016/j.polymer.2020.122882
39. Mieczkowski R (1992) Solubility parameter components of some polyurethanes. Eur Polym J 28(1):53–55. https://doi.org/10.1016/0014-3057(92)90237-v

Publisher's Note Springer Nature remains neutral with regard to jurisdictional claims in published maps and institutional affiliations.

Authors and Affiliations

Lucas Dall Agnol[1,2] · Marcos Gustavo de Medeiros Brandão[1] · Gricirene Sousa Correia[1] · Fernanda Trindade Gonzalez Dias[3] · Marco Sangermano[4] · Otávio Bianchi[2]

✉ Lucas Dall Agnol
lucas.agnol@ifma.edu.br

✉ Otávio Bianchi
otavio.bianchi@gmail.com

[1] Postgraduate Program in Materials Science and Technology (PPGCTM), Federal Institute of Education, Science and Technology of the State of Maranhão, São Luis, MA, Brazil

[2] Department of Materials Engineering (DEMAT), Federal University of Rio Grande Do Sul (UFRGS), Porto Alegre, RS, Brazil

[3] Postgraduate Program in Materials Science (PPGCIMAT), Federal University of Rio Grande Do Sul (UFRGS), Porto Alegre, RS, Brazil

[4] Department of Applied Science and Technology, Politecnico Di Torino, C.So Duca Degli Abruzzi 24, 10129 Turin, Italy